Ultra-Broadband Shielding of Cellulose Nanofiber Commingled Biocarbon Functional Constructs: A Paradigm Shift Towards Sustainable Terahertz Absorbers

*Avinash R. Pai[a,d], Yuezhen Lu[d], Saju Joseph[b], Neelakandan M. Santhosh[c], Riccardo Degl'Innocenti[d], Hungyen Lin[d], Rosa Letizia[d], Claudio Paoloni[d], Sabu Thomas[a,b]**

[a]International and Inter University Centre for Nanoscience and Nanotechnology, Mahatma Gandhi University, Kottayam, Kerala-686560, India

[b]School of Nanoscience and Nanotechnology, Mahatma Gandhi University, Kottayam, Kerala 686560, India

[c]Department of Gaseous Electronics (F6), Jožef Stefan Institute, Jamova cesta 39, 1000 Ljubljana, Slovenia

[d]School of Engineering, Lancaster University, Lancaster, LA1 4YW, United Kingdom.

Corresponding Email: sabuthomas@mgu.ac.in

Graphical Abstract

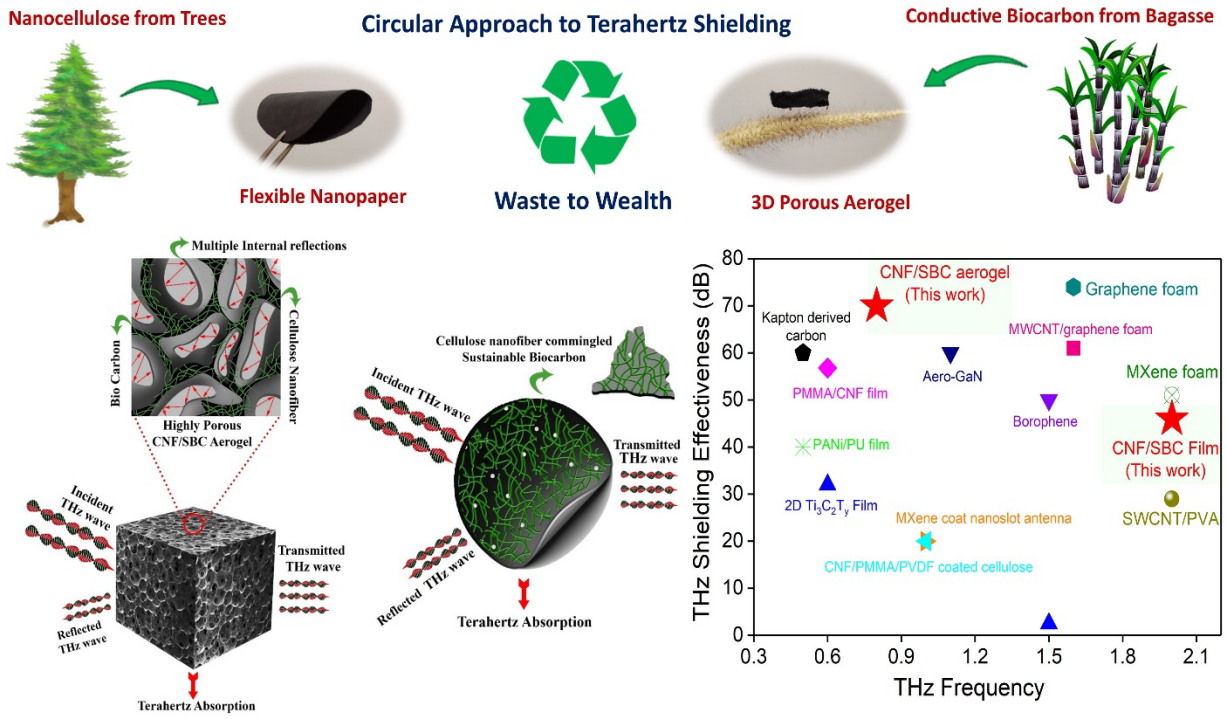

Abstract

Terahertz (THz) spectrum and technology are envisioned to be a highly promising solution for enabling 6G and beyond wireless networks. This demand coincides with an urgent need to develop efficient electromagnetic interference shields to alleviate electromagnetic pollution in the THz range. Fully bioderived THz shields could be a sustainable solution to transcend towards a biocarbon economy. Herein, we report an environmentally benign and facile approach to fabricating 3D porous ultra-light aerogels and flexible nanopapers from cellulose nanofibers and highly conductive biocarbon fully derived from biomass. The THz shielding effectiveness of a 600 µm thick nanopaper and 3.00 mm aerogel was found to be 46 dB and 70 dB, with superior THz absorption behaviour and minimal reflection of THz signals. The electronic structure and charge transfer properties were examined under an external electric field based on density-functional theory. The results show that the effect of the external electric field induces intramolecular charge transfer from the lower-graphitic sheet to the upper-graphitic sheet of the nanocomposite suitable for THz excitation. Moreover, these sustainable

absorbers could deliver similar THz shielding performance compared to graphene foam (74 dB), exemplifying their humungous potential as an advanced functional materials for futuristic THz devices.

Keywords: Cellulose Nanofibers, Biocarbon, Electrical Conductivity, Terahertz Time Domain Spectroscopy, Terahertz Shielding, DFT Calculation.

1. Introduction

A new generation of electronic devices at THz frequencies is emerging for enabling applications in biomedical imaging[1], security screening[2], chemical analysis[3], spectroscopy[4], detectors[5][6], modulators[7] and high-speed communication systems[8]. The THz electromagnetic radiation covers the frequency range of 100 – 10000 GHz (0.1 - 10 THz). The outstanding properties of THz frequency have attracted the highest interest of the scientific community due to the wide unexplored band suitable for high data rate transmission [9]. The fast-growing applications of THz technology have led to an urgent demand for designing efficient THz shielding materials to prevent EMI and facilitate the smooth functioning of new THz devices. To this day, there are numerous reports of nanomaterials and composites, which demonstrate excellent shielding performance at MHz and GHz frequencies[10][11], but there are only a small number of reports on high-performance shielding materials in the THz range.

The most widely explored THz shielding materials are based on conductive nanomaterials, such as graphene, carbon nanotubes (CNTs), MXenes and their flexible polymer nanocomposites. Recently, Choi *et al*. fabricated a combination of ultra-thin MXene film-coated nanoscale slot antenna arrays and studied its attenuation performance in the THz region [12]. These hybrid antennas demonstrated a maximum shielding of 20 dB at 1.0 THz, which infers its potential application for optical switching and modulation. Using a multistep approach, Hou and co-

workers developed an array of flexible Cu/graphene nanocomposites grown on PI film and elucidated its THz shielding performance[13]. These flexible & ultrathin polymers-supported THz shields displayed an average EMI SE of 60.95 dB at 0.1–1.0 THz and 160 nm thickness. Furthermore, designing 3D porous architectures has proven to substantially reduce the density and enhance the EMI shielding performance across GHz & THz frequencies. This could be ascribed due to multiple internal scattering and trapping of incident EM radiations within the porous network, substantially increasing the microwave or THz absorption. Using this strategy, Huang *et al.* designed 3D graphene foams with ultra-broadband and wide-angle THz absorption characteristics [14]. At the incident angle of 45°, the maximum R_L value for 4 mm thick graphene foam touches 28.6 dB at 0.64 THz and showcases an R_L value of over 10 dB across a broad bandwidth from 0.2-1.2 THz. In another work, Lin *et al.* fabricated MXene foams with outstanding durability, foldability and hydrophobicity using an ion-diffusion-induced gelation method[15]. These foams exhibited superior terahertz shielding effectiveness of 51 dB at 85 μm thickness. Moreover, all the aforementioned works are based on exotic nanomaterials, which involve complex, multistep, time- and energy-intensive nanofabrication processes. To the best of our knowledge, no studies report facile approaches to fabricating fully sustainable and biodegradable THz shielding materials that can deliver superior EMI shielding performance in the THz range at par with their nano counterparts.

Nanocellulose, a renewable plant-derived bio-nanomaterial, is suitable for various applications ranging from biomedical to flexible electronics due to its excellent mechanical strength, chemical resistance, thermal stability and processability. These unique attributes of nanocellulose have been widely explored for designing efficient EMI shielding materials in GHz frequencies[16–19]. Conductive biochar is another renewable resource that has attracted great interest owing to its low bulk density, high surface area and tuneable porosities. The presence of graphite-like structures in biochar renders high electrical conductivity. It has been

widely explored for battery electrodes[20], sensors[21] and EMI shielding in GHz frequencies [22,23]. Hence, one can foresee the tremendous potential of combining nanocellulose and conductive biochar as a fully sustainable solution to screen undesired interference of THz waves for futuristic electronic devices functioning in this broad spectrum.

In this work, we aim to fabricate fully sustainable and biodegradable THz shielding materials from cellulose nanofibers (CNF) & sustainable biocarbon (SBC). Herein, a series of highly flexible nanopapers and 3D porous aerogels were fabricated via facile processing techniques, i.e. vacuum filtration and lyophilisation. The CNF/SBC nanopaper exhibited a maximum electromagnetic interference shielding effectiveness (EMI SE) of 46.0 dB at 2.0 THz and 600 μm thickness. Moreover, a 3.00 mm thick 3D porous CNF/SBC aerogel displayed an exceptional EMI SE of around 70.0 dB at 0.8 THz. Interestingly, the nanopapers and aerogels demonstrated low reflection value, which infers superior THz absorption behaviour of these nanocomposite shields. In common practice, studying the THz shielding properties of nanostructured materials involves synthesising such structures and performing accurate THz physio-chemical experimental studies with sophisticated instruments, which can produce results with reasonable accuracy. However, the geometric, electronic, and interfacial charge transfer properties play a crucial role in nanocomposites consisting of multiple nanostructures. Here, in addition to experimental studies, we used first-principles density functional theory (DFT) calculations to examine the optoelectronic and charge transfer properties of graphite-like biocarbon-nanocellulose nanocomposite (CNF/SBC) structures. To the best of our knowledge, this is so far the first report of fully biodegradable THz absorbers derived from biomass to touch 70 dB (>99.99999% shielding) in the THz range, which will create a positive impact on the environment in the near future and promote circular economy.

2. Materials & Methods

2.1 Synthesis of Sustainable Biocarbon (SBC)

Highly conductive, short-range ordered graphitic biocarbon was fabricated by converting agricultural waste biomass such as sugarcane bagasse. Initially, waste biomass was collected from nearby farmland and chopped into small pieces 0.5 mm in length. About 100 gm of chopped bagasse dispersed in 50 ml distilled water was transferred into a teflon-lined hydrothermal (HT) reactor and heated up to 200°C at a heating rate of c.a. 5 °C/min for 24 hrs. In this process, biomass residue was partially carbonised under self-generated temperature and pressure inside the reactor to form wet hydrothermal carbon. The wet HT carbon was freeze-dried at -80°C for 24 hours to remove the excess water content. The dry HT carbon was further subjected to pyrolysis at 900°C for 4 hrs in an N_2 atmosphere to form highly conductive SBC with intriguing physical and electrical properties

2.2 Fabrication of CNF/SBC-Aerogels and Nanopapers

Herein, we fabricated a series of highly conductive nanopapers and aerogels from SBC and CNF using environmentally benign pathways without any organic solvents. Initially, the calculated amount of SBC was added to 100 ml distilled water and the probe was sonicated for 25- 30 mins to form a stable suspension of aqueous SBC. For the preparation of SBC/CNF nanopapers, SBC suspension was added to 20 gm of CNF (1 wt%) and homogenised at 8000 rpm to facilitate proper dispersion of SBC. This was followed by vacuum filtration and hot pressing at 80°C to form flexible and conductive CNF/SBC nanopapers. In another protocol, the SBC suspension was added to 20 gm of CNF (3 wt%) and homogenised at 8000 rpm, followed by freeze-drying the suspension at -80°C for 48 hours to form a lightweight and highly conductive SBC/CNF aerogels. The CNF: SBC ratio formulated in this study was 1:1, 1:2.5 and 1:5 on a weight basis for both nanopapers and aerogels.

2.3 Physico-Chemical Characterisation

The morphology of the nanopapers and aerogels were studied by probing the surface and cross-sections under a field emission scanning electron microscope (FESEM: ZEISS Gemini 300

SEM) with an accelerating voltage of 15 kV. Prior to imaging, all the samples were cryo-fractured in liquid N_2 and sputtered with gold under an inert atmosphere. The high-resolution transmission electron microscopy (HR TEM: JEOL JEM-2100) imaging was performed to elucidate the turbostatic structure of SBC and nano-fibrillated networks of CNF. The DC conductivity studies of CNF/SBC samples were performed using a four-probe set-up with gold probes coupled to Keithley 2400 source meter, and the measurements were taken at room temperature. The Fourier Transform Infrared (FTIR) spectra of neat CNF, SBC and CNF/SBC compositions were recorded in transmission mode using ATR-FTIR (Shimadzu) with a resolution of 4 cm^{-1} and 15 scans in the range 500-4000 cm^{-1}. The X-Ray diffractograms of all the samples were recorded at ambient conditions using Shimadzu XRD-6000 within a 2ɵ range, 5 to 40° and a scan rate of 2° min^{-1}. The thermal stability of all the samples was performed using SDT Q600 Thermogravimetric Analyzer (TGA), TA instruments. The surface compositional analysis of SBC was performed using an Axis Ultra-DLD system, Kratos Analytical X-Ray photoemission spectrometer (XPS) with Al Kα X-ray source (hν = 1486.8 eV) over a binding energy range of 0–900 eV. The Raman spectra were recorded using an alpha300 R Confocal Raman Microscope (WITec GmbH).

2.4. Sub-Tera Hertz Shielding Measurements

The sub-THz electromagnetic interference shielding performance of the fabricated CNF/SBC nanopapers and aerogels was measured using a Vector Network Analyzer (model: R&S ZVA 40) with extenders for measurements in the W band frequency region (75 to 110 GHz). The classical waveguide method was used to measure the absorption characteristic in this range, where transmission and reflection measurements were obtained between two open-end WR-10 rectangular waveguides (Figure S1)[24]. Given the thin nature of the samples (thickness $\ll \lambda/2$), these were placed between the two waveguide flanges. The scattering parameters of the samples were obtained, and the total EMI SE values were calculated using standard equations[25].

2.5 Terahertz Shielding Measurements

The THz shielding performance, absorption and reflection values of the CNF/SBC nanopapers and aerogels were evaluated at room temperature using a commercial THz-TDS set-up (TERA K15, Menlo Systems, Germany) in both transmission and reflection geometry. When used in reflection configuration, THz radiation was focused and collected using four Au-coated parabolic mirrors with a 5 cm focal length. The incident angle was kept fixed at approximately 30 deg. The samples were always positioned in the focus of the optical transmission and reflection set-ups while recording the transmitted/reflected radiation at the different relative positions, thus acquiring a THz map of the different materials. The THz spot size in focus was in both configurations ~ 1 mm^2. A flat, highly reflective metallic sample was used as the reference in reflection configuration, whilst the air was used to normalise the acquired waveforms in transmission.

3. Results and Discussion

3.1. Morphology and Chemical Features

Advanced cellulose-based hybrid nanoarchitectures for high-performance THz EMI shielding were designed by an environmentally benign two-stage approach. In the first stage, highly conductive and sustainable biocarbon (SBC) was synthesized from lignocellulosic waste biomass as illustrated in **Figure 1(a).** In this work, sugarcane bagasse was pyrolyzed to produce highly conductive graphite like carbon via a two-step carbonization process. Subsequently, flexible nanopapers and lightweight aerogels were fabricated by commingling SBC with cellulose nanofibers by vacuum filtration and freeze-drying techniques as depicted in **Figure 1(b).** To discern the effect of SBC concertation on THz attenuation, aerogels and flexible papers were fabricated at three different concentrations of SBC with CNF. Though waste biomass are utilized for producing heat energy by incineration, their potential for developing more value-added materials like conductive biocarbon for high end applications has not been widely

explored. Therefore, it is important to understand the structural, chemical and compositional characteristics of SBC that could influence the THz shielding performance.

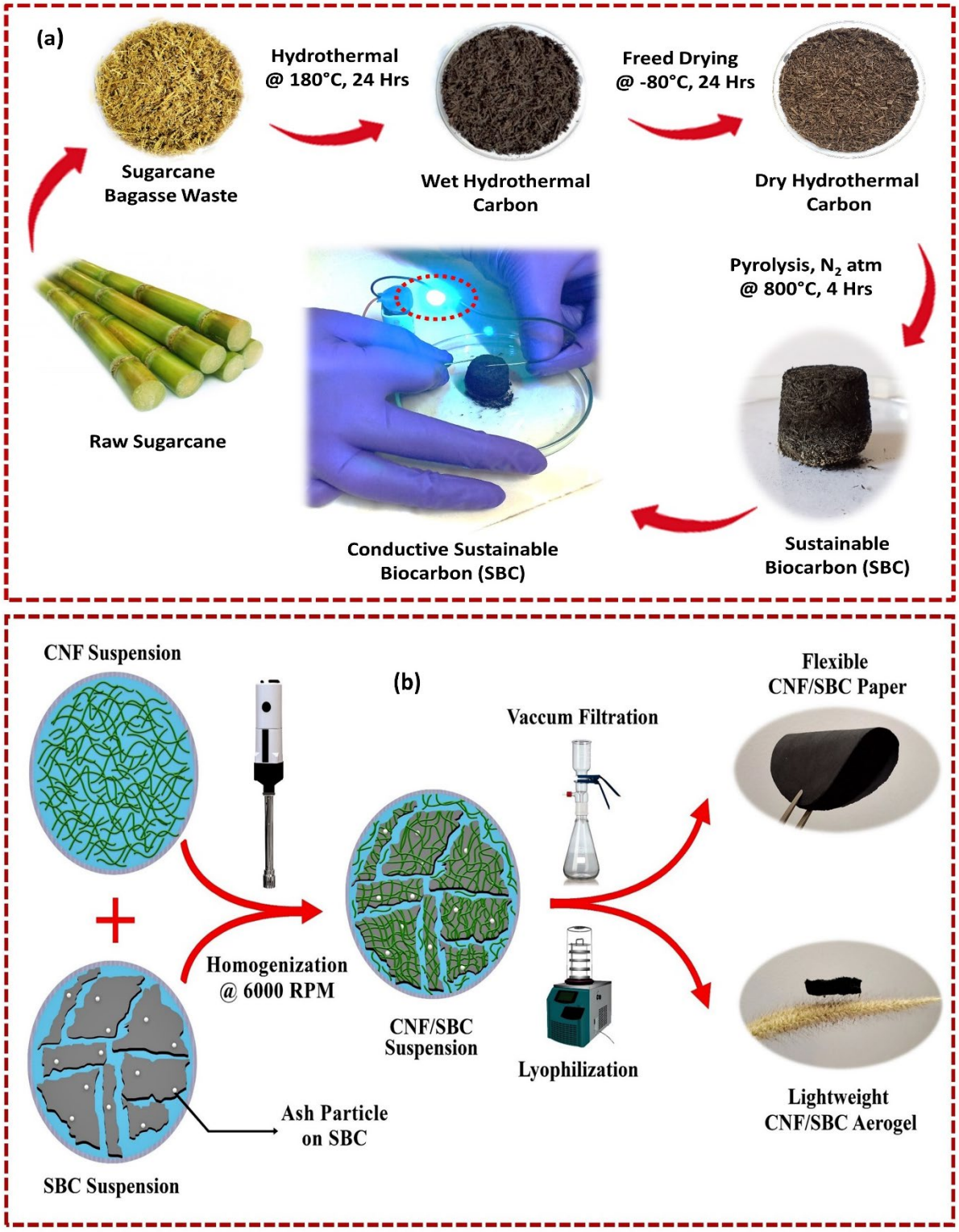

Figure 1: (a) Schematic diagram illustrating fabrication of sustainable biocarbon (SBC); (b) Fabrication of CNF/SBC aerogels and nanopapers.

197 The physical and chemical properties of the fabricated SBC were analysed by different
198 spectroscopic techniques. In order to identify the structural quality of SBC, Raman spectra were
199 recorded on the structures. The Raman spectra of SBC featured two main peaks corresponding
200 to the characteristic peaks observed in graphitic carbon materials. The D peak was observed
201 around 1350 cm^{-1}, attributed to the A_{1g} breathing mode of six-atom rings at the 1st Brillouin
202 zone boundary K or K'. This peak becomes active only in structural defects, where a charge
203 carrier must be excited and possess inelastic scattering by phonon. Then, a second elastic
204 scattering occurs by the defects, resulting in recombination. The second peak, the G band at
205 ~1590 $cm^{-1,}$ corresponds to the graphitic peak due to the one-phonon Raman scattering process
206 at the 1st Brillouin zone centre and consists of the collective in-plane bond stretching of carbon
207 atoms (E_{2g} symmetry). In addition to these main peaks, a broad 2D band at ~2700 cm^{-1} is visible,
208 attributed to the second-order of the D band originating from the scattering by two phonons
209 with opposite wave vectors. A small intense D+G peak is also visible around 2860 cm^{-1}. The
210 presence of D and G peaks along with the 2D peaks indicates the graphitic characteristics of
211 the material; hence the broad D and 2D features indicate the low concentration of the amorphous
212 phase of multi-layered carbon nanostructures. To give an insight into the structural defects in
213 the prepared carbon nanostructure, the intensity ratio between the D peak and G peak was
214 calculated (I_D/I_G ratio), which is directly proportional to the defect density of the graphitic
215 carbon material. The D and G peaks were fitted using the Lorentzian function, and the ratio was
216 calculated as 0.77 by considering the intensity of the peaks (**Figure 2 (a**)). Besides the D and
217 G bands, two minor peaks that appeared during the fitting correspond to the disordered carbon
218 in the lattice, possibly due to the amorphous phase in the material. The chemical composition
219 analysis of the sample was done to understand better the structural quality of the material using
220 XPS analysis. High-resolution C 1s spectra are presented in **Figure 2 (c)**. C 1s spectra were
221 deconvoluted into different peaks at 284.6, 285.8, 286.4, 287.2, 289, 290.9 and 284 eV. These
222 peaks can be ascribed to the graphitic-C (sp^2 C-C), sp^3 C-C, C-OH, C=O, π-π* shake-up satellite

groups and vacancy defects. The deconvoluted peaks in C 1s spectra confirm the high graphitic content in the samples due to the presence of dominant sp^2 c-c bonds and π-π* shake-up satellite groups.

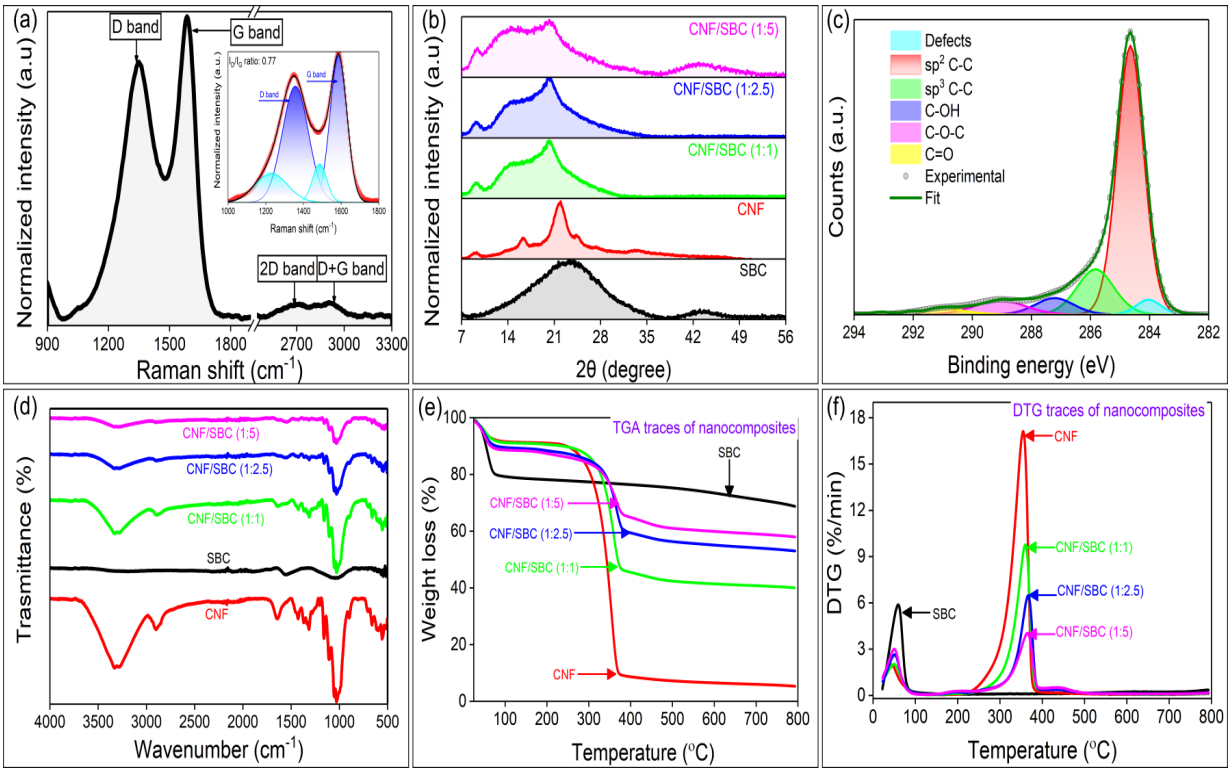

Figure 2: Characterisation of biocarbon and CNF/SBC functional constructs (a) Raman spectra of SBC samples with fitted D and G band and the calculated value of I_D/I_G ratio (inset); (b) XRD pattern (c) high-resolution C 1s spectra of SBC**;** changes in structural and chemical composition as a function of CNF/SBC ratio (d) FTIR fingerprints (g) TGA trace and (h) DTG trace.

The structural alterations of SBC after blending with CNF as a function of the concentration were further analysed by X-ray diffraction. The XRD pattern of SBC, as seen in **Figure 2(b)**, demonstrates that two broad and low-intensity diffraction peaks correspond to low crystallinity. The 2θ peaks at diffraction angles of ~23° (002) and ~44° (100) confirm the formation of a graphite-like structure in SBC. The peak at the (100) plane is representative of the graphite basal plane, and the (002) plane signifies the spatial organisation perpendicular to the basal

238 plane, which confirms the staking of graphitic layers [26]. In the case of CNF/SBC
239 nanocomposites, with increasing SBC content, the peak at 23° shifts towards a lower angle and
240 is envisaged due to the intercalation of CNF into the interlayers of SBC, thereby increasing the
241 d spacing of SBC in these nanocomposites. The FTIR spectra of SBC, CNF and their
242 nanocomposites is shown in **Figure 2(d)**. Due to the graphitisation process occurring during
243 pyrolysis, the FTIR spectra of SBC almost resemble that of graphite which has no characteristic
244 infrared bands [27]. The FTIR spectra of pristine CNF show characteristic bands at 3350, 2885,
245 1639, 1438, 1331, 1171, 1035 & 889 cm^{-1}. The peak at 3350 cm^{-1} arises due to O-H stretching,
246 and the bands at 2885 & 1639 cm^{-1} can be attributed to the C-H stretching and H-O-H bending
247 of the water molecules adsorbed onto CNF. The peaks at 1331 & 1171 cm^{-1} are ascribed to O-
248 H bending and C-O antisymmetric bridge stretching. A strong band around 1035 cm^{-1} is due to
249 C-O-C pyranose ring skeletal vibrations in the CNF backbone[28]. However, upon
250 carbonisation above 800°C, these functionalities tend to vanish due to dehydration and aromatic
251 condensation to form carbonaceous chars with a high carbon content of c.a. 80-90%. Thus, the
252 FTIR spectra of SBC display only two peaks at around 1500-1600 cm^{-1}, which corresponds to
253 C=C vibrations in aromatic rings. The 2nd peak at 1500-1600 cm^{-1} can be ascribed due to C–O
254 stretching vibrations or C–H out-of-plane bending in aromatic moieties [29,30]. The thermal
255 and chemical stability of these bio-nanocomposites is critical for practical applications. The
256 TGA/DTG thermograms of SBC and CNF/SBC nanocomposites depicted in **Figure 2 (e,f)**
257 demonstrates their thermal stability. The onset degradation temperature for all the compositions
258 was enhanced upon the addition of SBC, which resembles its excellent thermal stability. All
259 samples demonstrated a two-step degradation process, an initial weight loss of around 100°C,
260 due to low molecular volatiles or moisture loss, which arises due to the hygroscopic nature of
261 bio-carbon and CNF. A sharp weight loss around 350°C was observed due to the degradation
262 of cellulose structure, where SBC shows no sign of weight loss in this range[31]. Notably, the
263 degradation rate and weight loss of these nanocomposites decreased with the addition of bio-

carbon. Moreover, with increasing SBC concentration, the residue/char content of CNF/SBC also increases, which infers that SBC enhances the thermal stability of these nanocomposites. All the chemical and structural analyses confirm the formation of carbon nanostructures with high graphitic components after the calcination process with high stability.

In order to understand the morphology changes of SBC, CNF/SBC aerogels and nanopapers, the structure was analysed by FE-SEM and the changes observed on the surfaces are presented in **Figure 3 (a-i).** The SEM micrographs were taken at different magnifications to probe into the finer surface details of the biocarbon and its nanocomposites. It could be observed that SBC exhibited a flake-like morphology with a high degree of porosity, and ash particles were seen as overgrown on its surface. For CNF/SBC aerogels, the formation of a 3D porous network of CNF and SBC was evident from the surface of the aerogels. In the case of nanopaper, unlike aerogels, SBC and CNF were compactly packed on the surface, which could be due to the vacuum filtration and hot-pressing process employed during the synthesis process. However, as observed from the higher magnification SEM micrographs, both CNF/SBC nanopapers and aerogels showcased that cellulose nanofiber was well interconnected and blended on the surface of biocarbon, which signifies good interaction between CNF and SBC. Therefore, the HR-TEM micrograph was used to analyse the nanostructured features (**Figure 3(j)**) of biocarbon, and it clearly demonstrates the turbostratic, highly distorted and condensed carbonaceous nanostructures present in SBC[32]. The selected area electron diffraction (SAED) pattern (**Figure 3(k)**) indicates two diffused rings which correspond to (100) and (002) planes representing graphite-like carbon. The TEM image of CNF (**Figure 3(l)**) used herein shows the nanofibrous network of cellulose with an average fibre diameter of 20-30 nm. All the structural and compositional analysis confirms the production of highly stable, lightweight bio-based graphitic carbon composites.

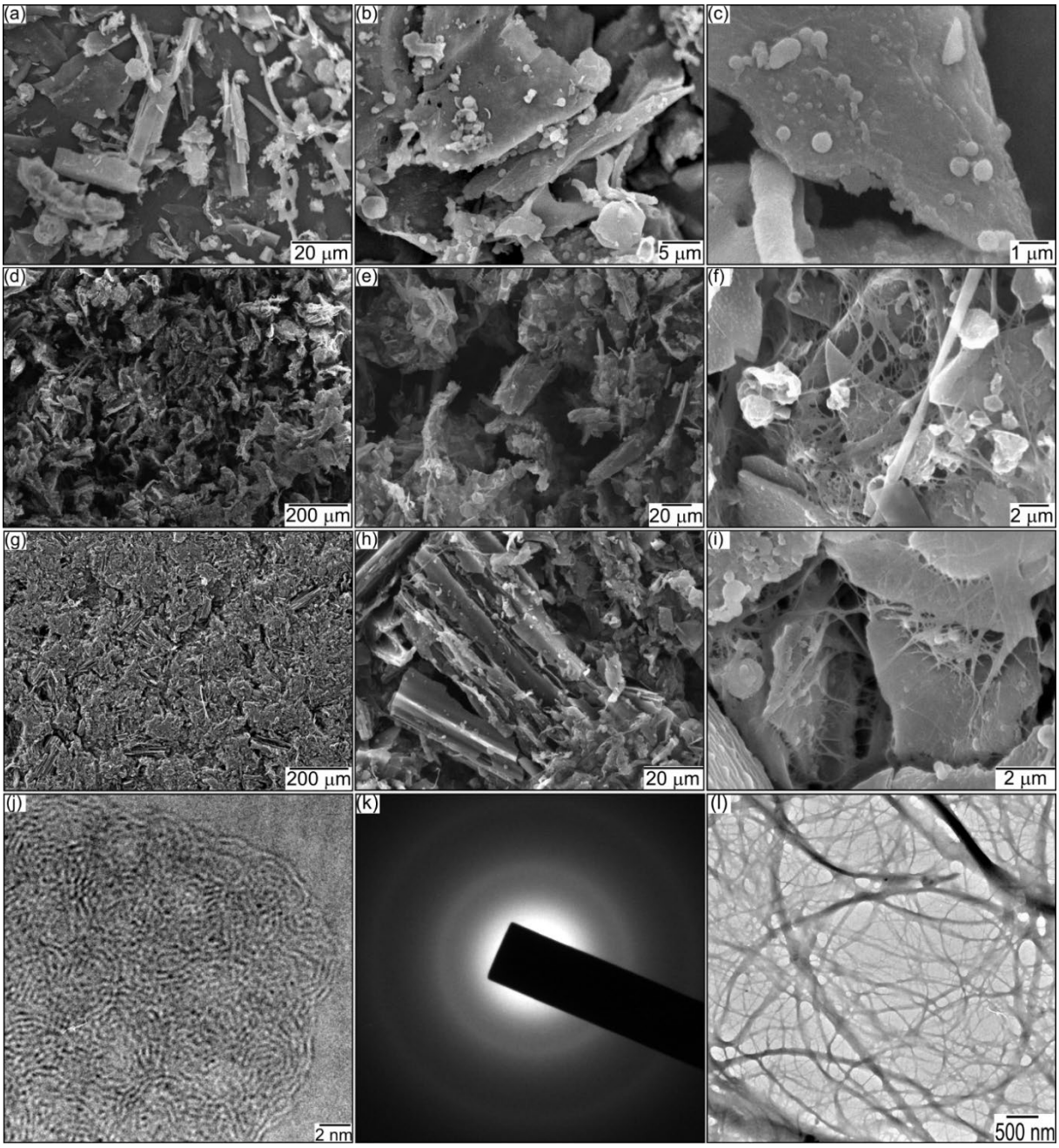

Figure 3. Surface morphology and structural organisation of prepared functional constructs. Overview and high magnification FE-SEM micrographs of (a, b, c) SBC (d, e, f) 1:5 CNF/SBC aerogel and (g, h, i) 1:5 CNF/SBC nanopaper; (j) HR-TEM micrograph of SBC (k) SAED pattern of SBC (l) TEM micrograph of CNF.

3.2. Sub-THz Shielding Performance of CNF/SBC Aerogels and Nanopapers

The sub-THz shielding performance of all the designed functional constructs was evaluated in W band (75-110 GHZ) region using a vector network analyser (VNA). The SE_A, SE_R and SE_{Total} shielding values of CNF/SBC aerogel and nanopaper at different SBC concertation are shown in **Figure 4(a-f)**. With increasing SBC content, the EMI SE values of both aerogel and nanopaper remarkably increased, which confirms the ability of these conductive nanocomposites to screen EM radiations.

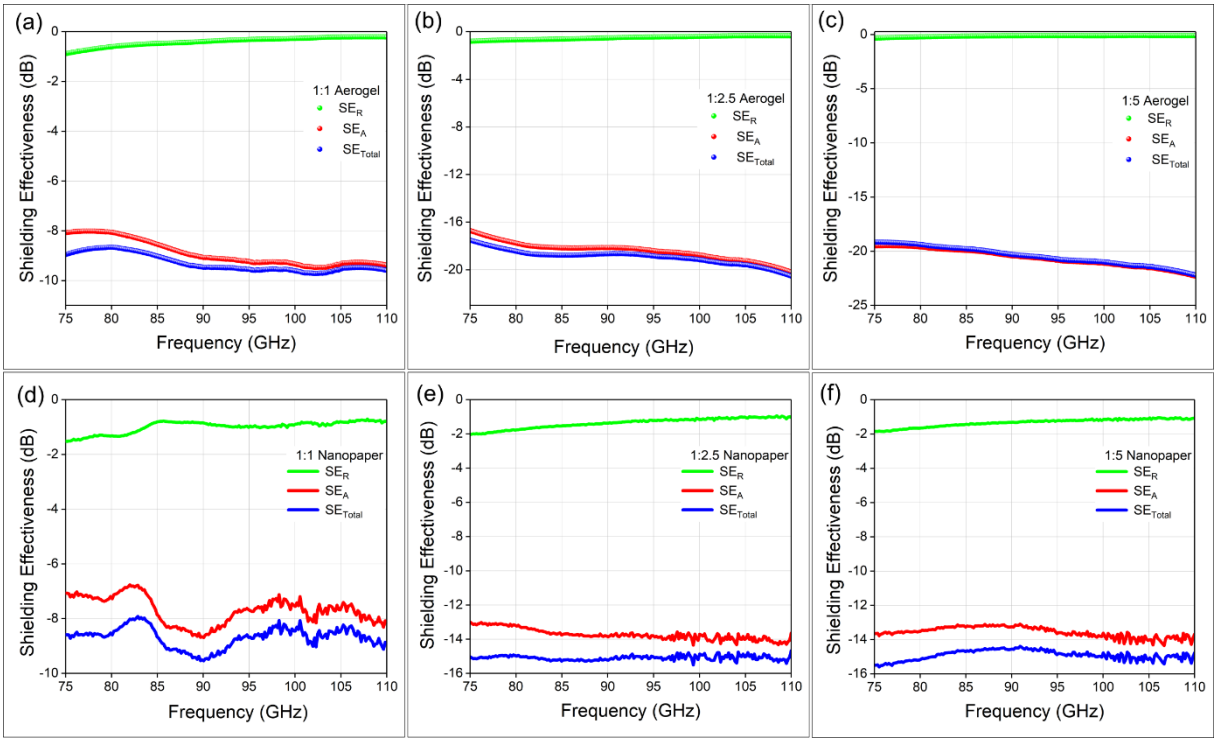

Figure 4. The shielding effectiveness values of (a) 1:1 (b) 1:2.5 & (c) 1:5 CNF/SBC aerogel (d) 1:1 (e) 1:2.5 & (f) 1:5 nanopaper in W band (75-110 GHz) region.

The maximum shielding effectiveness @90 GHz recorded for the nanopaper and aerogel was ca. -14.5 dB & -20.5 dB for 1:5 composition. The porous architecture of the aerogel was found to enhance the EM absorption and overall shielding value due to better impedance matching and more incidents of multiple internal scattering inside the aerogel. It is also noteworthy that both the CNF/SBC nanopaper and aerogel showcased minimal shielding due to a reflection

value of less than -2 dB, which infers the predominant absorbent nature of these biodegradable functional constructs with superior broadband EM absorption characteristics.

3.3. Terahertz Shielding Performance of CNF/SBC Aerogels and Nanopapers

The THz shielding performance of these functional constructs were evaluated in transmission mode (**Figure 5(a)** by measuring the intensity and phase of the THz signals.

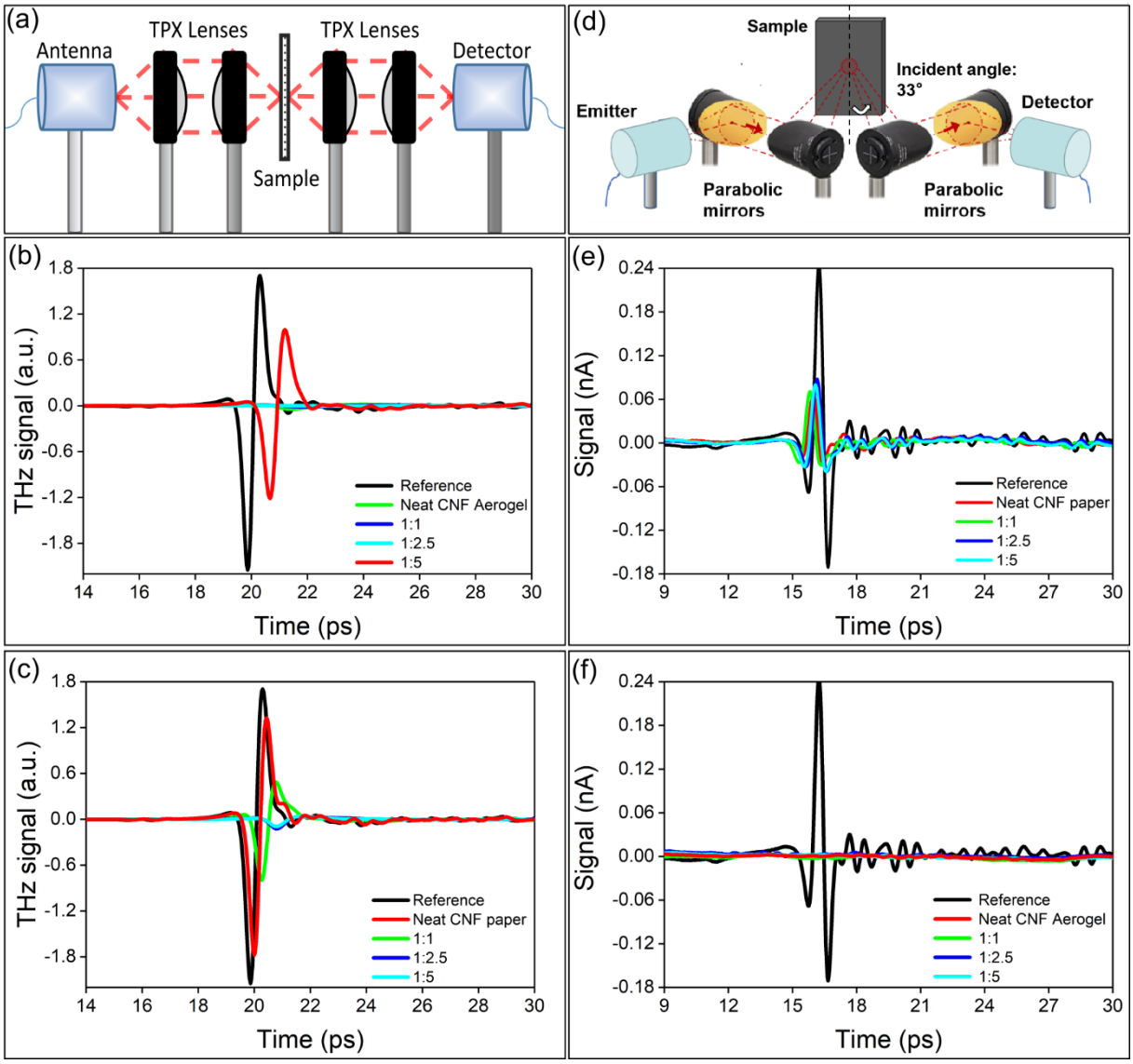

Figure 5. THz shielding performances of the designed hybrid structures (a) Transmission mode set-up of THz-TDS system and time domain response of (b) CNF/SBC aerogels & (c) CNF/SBC nanopapers at different CNF: SBC ratios in transmission mode (d) Reflection mode

set-up of THz-TDS system and time domain response of (e) CNF/SBC nanopapers & (f) CNF/SBC aerogels at different CNF: SBC ratios in reflection mode**.**

The time domain spectra of all the samples infer that the transmitted THz amplitude of CNF/SBC aerogel is smaller than that of the nanopaper with similar SBC concentration (**Figure 5(b,c)).** It is noteworthy that, for 1:5 aerogel, the intensity of the THz signal becomes almost negligible, confirming the high THz shielding ability of CNF/SBC aerogels when compared with nanopaper of similar concentration. Apart from improving the THz shielding performance, these highly porous aerogels also mitigate surface reflection and suppress further secondary pollution. In order to quantify the THz reflection from the surface, samples were measured in reflection mode, as shown in **Figure 5(d).** The intensity of the reflected signal for the aerogels was minimal compared to nanopapers of similar SBC content (**Figure 5(e-f)**). This also infers that CNF/SBC aerogels have tremendous potential to scatter the THz signals within the highly conductive and porous network, thereby contributing to higher THz absorption.

The time domain THz signals were converted into corresponding scattering parameters (S_{11} and S_{12}) in the frequency domain and dB scale. The THz shielding effectiveness (SE_{Total}), shielding by reflection (SE_R) and shielding by absorption (SE_A) values of CNF/SBC aerogels and nanopapers in the range of 0.4 to 2.0 THz are shown in **Figure 6(a-f).** For a 600 μm thick nanopaper, a maximum THz shielding value of 46 dB was recorded with a menial SE_R value of less than 0.14 dB at a 1:5 ratio. However, for aerogels with similar SBC content, the THz shielding value increased to 70 dB at 3.0 mm thickness with SE_R values as low as 0.002 dB. At maximum SBC content, the SE_{Total} value of aerogel was almost 1.5 times higher than that of nanopaper, which infers the potential of these highly porous structures to enhance the THz shielding performance. The outstanding THz performances are also related to the electrical properties of the nanostructures. Therefore, the electrical conductivity of SBC and CNF/SBC nanocomposites were studied. The analysis demonstrates that the carbon precursor was

pyrolysed at 900°C, resulting in excellent DC electrical conductivity of 36.7 S/cm for SBC (**Movie S1**). At a 1:5 ratio, CNF/SBC nanopaper (**Movie S2**) and aerogel (**Movie S3**) also displayed high electrical conductivity values of 23.3 S/cm and 25.6 S/cm, respectively.

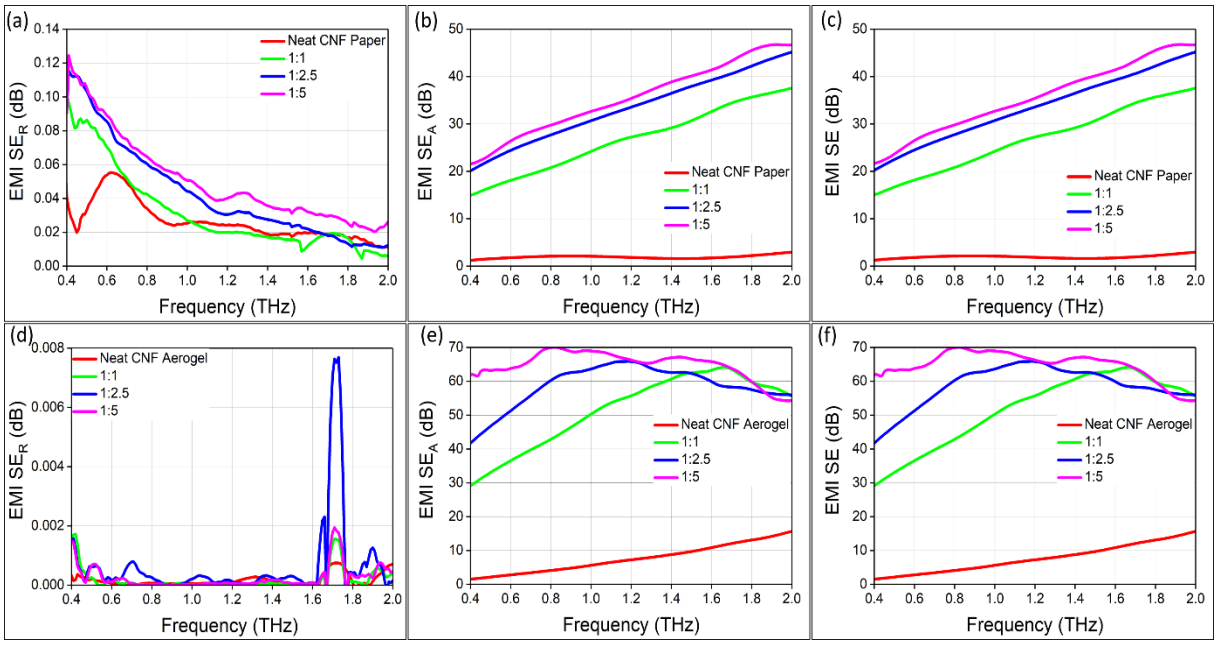

Figure 6. (a) Shielding by reflection (b) Shielding by absorption & (c) Total THz shielding effectiveness values of CNF/SBC nanopapers. (d) Shielding by reflection (e) Shielding by absorption & (f) Total THz shielding effectiveness values of CNF/SBC aerogels

Figure 7(a) presents the electrical conductivity demonstration of SBC, CNF/SBC nanopaper and aerogels by completing a closed circuit and lighting up LED using a 9V DC power supply, confirming the excellent electrical properties of these functional constructs. All these outstanding performances indicate that the CNF/SBC aerogel with excellent structural, electrical and optical features is an ideal candidate as a fully sustainable and biodegradable THz absorber. A comparison of the THz performance of these designed hybrid structures with the current reported materials is compared and presented in **Figure 7(b).** Interestingly, the total THz EMI SE value of CNF/SBC aerogel was almost similar to that of graphene foam (74 dB), indicating that these aerogels are a class of potential candidates for THz electronic devices. Based on all the findings and observations, a plausible mechanism in such structures was

identified, and a schematic representation of the THz shielding mechanism for CNF/SBC aerogel and nanopaper is depicted in **Figure 7(c).** It is worth noting that the underlying mechanism of THz shielding for both the nanopaper and aerogel is via predominant absorption of THz radiation and negligible reflection. In the case of aerogels, the incoming THz waves can undergo multiple internal scattering and interfacial polarisation within the 3D conductive porous architecture, which results in superior THz absorption than nanopaper [15,33].

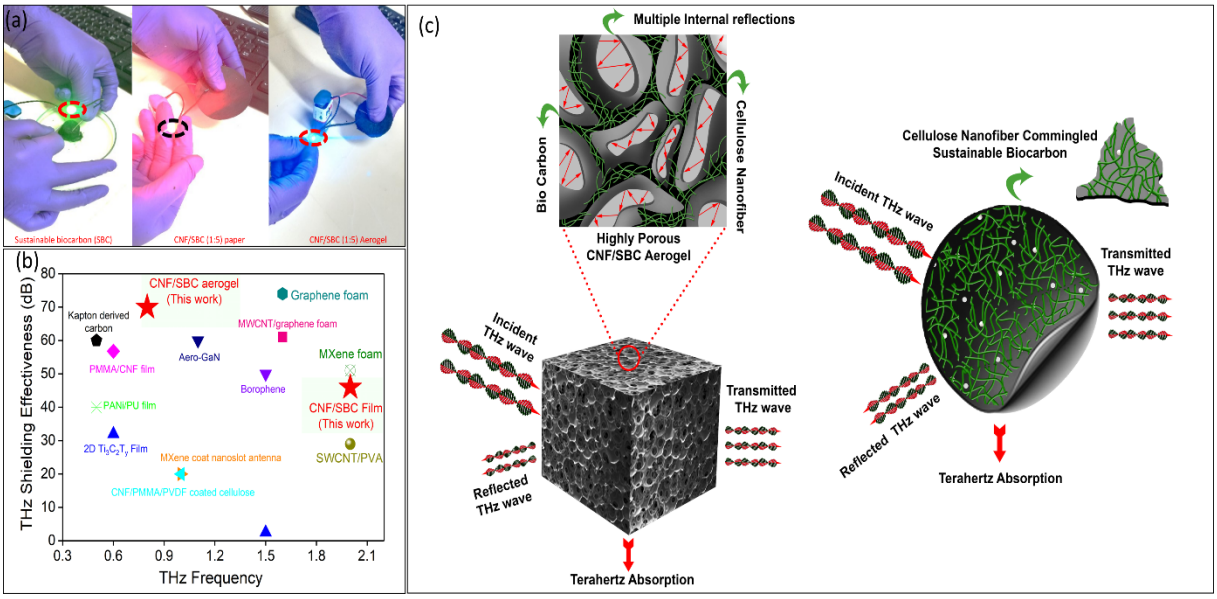

Figure 7. (a) Electric conductivity demonstration of SBC, 1:5 CNF/SBC nanopaper & 1:5 CNF/SBC aerogel using a LED and 9V DC power supply; (b) comparison of THz shielding effectiveness v/s THz frequency for state-of-the-art materials reported in the literature. (References in the graph are listed in **Table S1);** (c) a plausible THz shielding mechanism of CNF/SBC aerogel and CNF/SBC paper.

In order to identify the excellent THz performances and their correlation with the chemical structure of the hybrid structures, the charge-transfer (CT) states at the interface of the material were calculated by density functional theory. For a new nanostructured composite material, it is important to study its electronic structure and optoelectronic and charge transfer properties. Herein, the theoretical analysis of geometries, energetics, charge transfer, and optoelectronic

properties of graphite-like biocarbon, nanocellulose structure, and its nanocomposite (CNF/SBC) structure was evaluated using *ab initio-based* density functional (DFT) theory, with ωB97XD functional and 6-31G(d) basis set. Geometry optimisations and frequency calculations were carried out using DFT theory with the same level of theory; all the optimised structures gave no negative vibrational frequencies showing that all structures were minima on their potential energy surface. The optimised structures are illustrated in **Figure 8(a,b,c).**

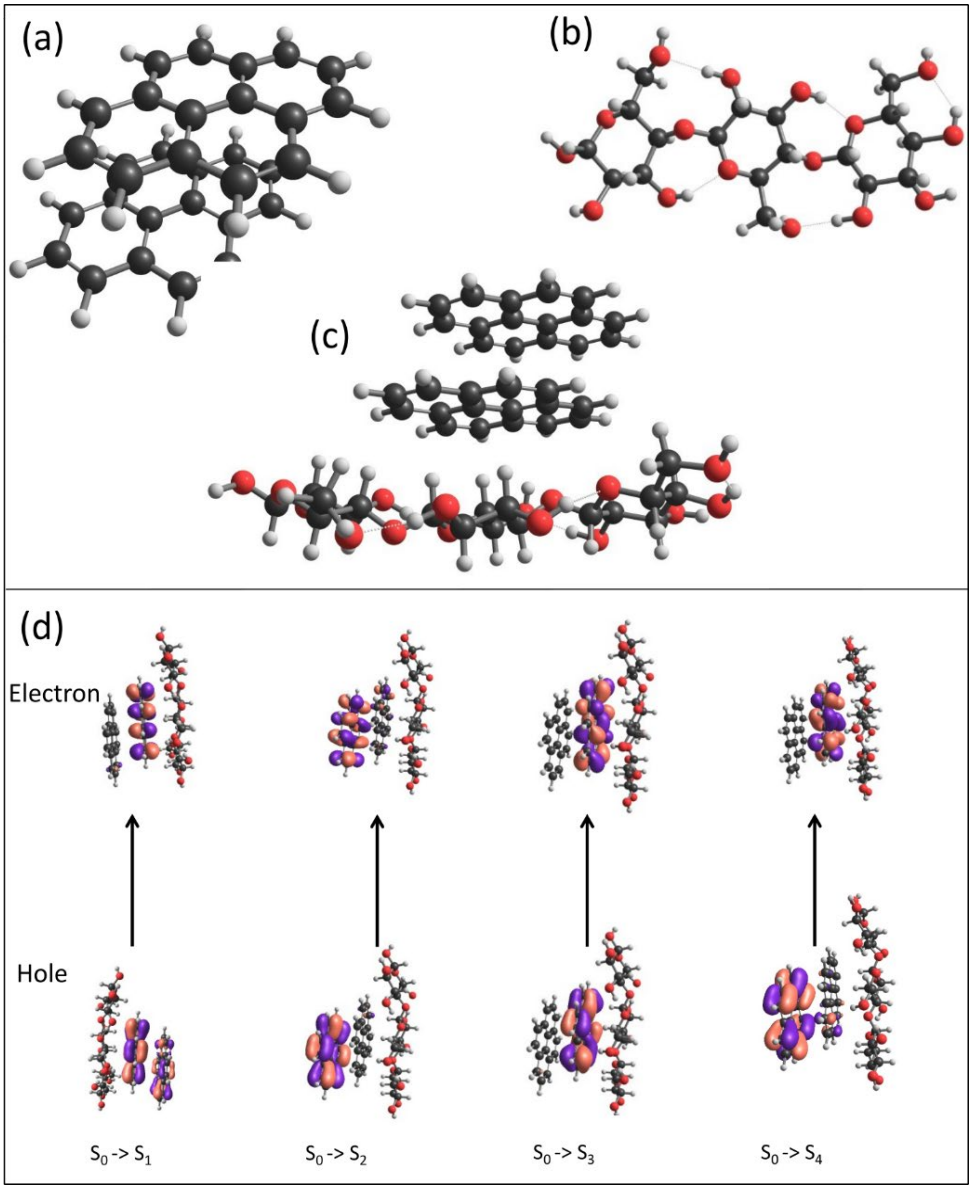

Figure 8: DFT-ωB97XD/6-31g(d) optimised structures: (a) graphite type cluster, (b) Nanocellulose, (c) graphite like bio-carbon/CNF nanocomposite (d) Lowest four excited states

of the graphite like bio-carbon/CNF nanocomposite calculated at the TD-ωB97XD/6-31g(d) level of theory.

The electric field was then applied to the optimised structures, and further relaxation of the molecular composite in the presence of the electric field was performed at the same level of theory. All the molecular modelling studies were carried out through the Gaussian 16 software package[34]. To compute the stability of the functional construct, we calculated the binding energy of the CNF/SBC nanocomposite as defined by the following equation:

$$E_{\text{bind}} = E_{\text{CNF/SBC}} - (E_{\text{CNF}} + E_{\text{SBC}}) + E_{\text{BSSE}} \quad (1)$$

The binding energy between graphite-like biocarbon and nanocellulose structure was computed at −19.9kcal/mol. A negative binding energy value indicates that the optimised nanocomposite is stable and energy-favourable and indicates the weak covalent interactions in the composite system. Due to the large computational requirements and mathematical complexity involved in using DFT for nanocomposite systems, we limited the system size of the composite to graphitic-type clusters (two units) and cellulose (three units) in our model.

Density functional theory has been proven to be extremely useful for predicting charge-transfer processes in molecular, ionic, composite, and complex systems[35–37]. For THz shielding applications, the charge-transfer (CT) states at the interface of the material play a major role in the performance of the nanocomposite shield. The nature of the excited states and the charge transfer state was investigated using a combination of time-dependent density functional theory (TD-DFT, ωB97XD/6-31G(d) level of theory) and Natural Transition Orbital (NTO) analysis. The first four lowest excited states of the CNF/SBC nanocomposite at the TD-DFT level of theory are depicted in **Figure 8(d),** along with the hole and electron wave functions obtained from an NTO analysis[38][39]. The first and fourth lowest excited states in these functional

constructs can be characterised as charge-transfer (CT) states. In contrast, the second and third excited states can be characterised as local-excited (LE) states of CNF/SBC nanocomposite.

Further, we have investigated the trends in molecular properties under the influence of an external electric field. The DFT results show that the effect of an external electric field induces intramolecular charge transfer (CT). We found that the electric field has little influence on the bandgap of the CNF/SBC construct. At the same time, it can induce an intramolecular charge transfer between the layers of the graphitic sheets which is of paramount importance in THz shielding performance. This observation is in good agreement with recent findings[40]. HOMO-LUMO orbitals (highest occupied molecule orbital to lowest unoccupied molecular orbital) distribution of the composite with an externally applied electric field are presented in **Figure S2**. The DFT results portray that the externally applied electric field components of the EM energy do interact with the permanent dipoles in this CNF/SBC functional constructs, and it induces intramolecular charge transfer (CT) from the lower-graphitic sheet to the upper-graphitic sheet of the CNF/SBC nanocomposites, with an increase in dipole moment. According to the DFT concept and their good agreement with experimental designs, CNF/SBC functional constructs were effective for designing high-performance THz shielding materials, which could open up a new paradigm for designing advanced THz shielding materials for next-generation device applications.

Conclusion

In this work, a series of biodegradable THz absorbers are demonstrated for the first time via facile processing techniques to produce highly conductive CNF/SBC aerogels and nanopapers purely derived from biomass. At a 1:5 ratio, these highly conductive aerogels & nanopapers displayed a maximum EMI SE of 70 dB at 0.8 THz and 46 dB at 2.0 THz. Interestingly, these functional THz shields predominantly absorb THz waves with the negligible reflection of

incoming signals. Moreover, the aerogel could deliver 1.52 times higher THz shielding performance than nanopapers. Due to the high porosity of aerogels, the incoming THz radiation gets scattered within the multiple interfaces of the conductive porous network and gets absorbed without generating any secondary reflection or further EM pollution. This work not only provides a facile approach to fabricating sustainable THz shielding materials for new-generation THz devices but also opens up possibilities for a plethora of other technological applications, such as strain sensing, water purification, energy storage and harvesting. Nevertheless, after the service life of these sustainable THz shields, they could be easily disposed of as manure for plants as the biocarbon would facilitate soil amendment, thereby sequestering carbon dioxide from the atmosphere and helping reduce global warming.

Acknowledgements

ARP and ST gratefully acknowledge the financial support from the Ministry of Electronics and IT (MeitY), Digital India Corporation, (Formerly Medialab Asia), New Delhi, India provided under the Visvesvaraya PhD Scheme (Ref No: PhD-MLA/4(58)/2015-16). ARP & CP would also like to thank the British Council, UK, for providing funding under the Newton Bhabha PhD Placement Programme 2019-20. RD and YL acknowledge support from EPSRC, Grant No. EP/S019383/1. YL acknowledges support from China Scholarship Council (CSC), No.202108890030. HL acknowledges the financial support from the Royal Academy of Engineering under the Industrial Fellowships program. We thank Borregaard (Sarpsborg, Norway) for sponsoring Exilva grade cellulose nanofibers.

References

[1] A. Rahman, A.K. Rahman, D.A. Tomalia, Engineering dendrimers to produce dendrimer dipole excitation based terahertz radiation sources suitable for spectrometry, molecular and biomedical imaging, Nanoscale Horizons. 2 (2017) 127–134.

[2] L. Ho, M. Pepper, P. Taday, Terahertz spectroscopy: Signatures and fingerprints, Nat. Photonics. 2 (2008) 541–543.

[3] Y. Shao, Y. Wang, D. Zhu, X. Xiong, Z. Tian, A. V. Balakin, A.P. Shkurinov, D. Xu, Y. Wu, Y. Peng, Y. Zhu, Measuring heavy metal ions in water using nature existed microalgae as medium based on terahertz technology, J. Hazard. Mater. 435 (2022) 129028.

[4] H. Shigekawa, S. Yoshida, O. Takeuchi, Nanoscale terahertz spectroscopy, Nat. Photonics. 8 (2014) 815–817.

[5] L. Vicarelli, M.S. Vitiello, D. Coquillat, A. Lombardo, A.C. Ferrari, W. Knap, M. Polini, V. Pellegrini, A. Tredicucci, Graphene field-effect transistors as room-temperature terahertz detectors, Nat. Mater. 11 (2012) 865–871.

[6] R. Degl'Innocenti, L. Xiao, D.S. Jessop, S.J. Kindness, Y. Ren, H. Lin, J.A. Zeitler, J.A. Alexander-Webber, H.J. Joyce, P. Braeuninger-Weimer, S. Hofmann, H.E. Beere, D.A. Ritchie, Fast Room-Temperature Detection of Terahertz Quantum Cascade Lasers with Graphene-Loaded Bow-Tie Plasmonic Antenna Arrays, ACS Photonics. 3 (2016) 1747–1753.

[7] R. Degl'innocenti, H. Lin, M. Navarro-Cía, Recent progress in terahertz metamaterial modulators, Nanophotonics. 11 (2022) 1485–1514.

[8] Y. Yang, Y. Yamagami, X. Yu, P. Pitchappa, J. Webber, B. Zhang, M. Fujita, T. Nagatsuma, R. Singh, Terahertz topological photonics for on-chip communication, Nat. Photonics. 14 (2020) 446–451.

[9] X.C. Zhang, A. Shkurinov, Y. Zhang, Extreme terahertz science, Nat. Photonics. 11 (2017) 16–18.

[10] Z. Zeng, F. Jiang, Y. Yue, D. Han, L. Lin, S. Zhao, Y.B. Zhao, Z. Pan, C. Li, G. Nyström, J. Wang, Flexible and Ultrathin Waterproof Cellular Membranes Based on High-Conjunction Metal-Wrapped Polymer Nanofibers for Electromagnetic Interference Shielding, Adv. Mater. 32 (2020) 1908496.

[11] J. Liu, L. Mckeon, J. Garcia, S. Pinilla, S. Barwich, M. Möbius, P. Stamenov, J.N. Coleman, V. Nicolosi, Additive Manufacturing of Ti3C2-MXene-Functionalized Conductive Polymer Hydrogels for Electromagnetic-Interference Shielding, Adv. Mater. 34 (2022) 2106253.

[12] G. Choi, F. Shahzad, Y.M. Bahk, Y.M. Jhon, H. Park, M. Alhabeb, B. Anasori, D.S. Kim, C.M. Koo, Y. Gogotsi, M. Seo, Enhanced Terahertz Shielding of MXenes with Nano-Metamaterials, Adv. Opt. Mater. 6 (2018) 1701076.

[13] S. Hou, W. Ma, G. Li, Y. Zhang, Y. Ji, F. Fan, Y. Huang, Excellent Terahertz shielding performance of ultrathin flexible Cu/graphene nanolayered composites with high

stability, J. Mater. Sci. Technol. 52 (2020) 136–144.
[14] Z. Huang, H. Chen, Y. Huang, Z. Ge, Y. Zhou, Y. Yang, P. Xiao, J. Liang, T. Zhang, Q. Shi, G. Li, Y. Chen, Ultra-Broadband Wide-Angle Terahertz Absorption Properties of 3D Graphene Foam, Adv. Funct. Mater. 28 (2018) 1704363.
[15] Z. Lin, J. Liu, W. Peng, Y. Zhu, Y. Zhao, K. Jiang, M. Peng, Y. Tan, Highly Stable 3D Ti3C2Tx MXene-Based Foam Architectures toward High-Performance Terahertz Radiation Shielding, ACS Nano. 14 (2020) 2109–2117.
[16] D.A. Gopakumar, A.R. Pai, Y.B. Pottathara, D. Pasquini, L.C. de Morais, A. Khalil H.P.S., A. Nzihou, S. Thomas, Flexible papers derived from polypyrrole deposited cellulose nanofibers for enhanced electromagnetic interference shielding in gigahertz frequencies, J. Appl. Polym. Sci. 138 (2021) 50262.
[17] A.R. Pai, C. Paoloni, S. Thomas, Nanocellulose-based sustainable microwave absorbers to stifle electromagnetic pollution, in: Nanocellulose Based Compos. Electron., Elsevier, 2021: pp. 237–258.
[18] D.A. Gopakumar, A.R. Pai, Y.B. Pottathara, D. Pasquini, L. Carlos De Morais, M. Luke, N. Kalarikkal, Y. Grohens, S. Thomas, Cellulose Nanofiber-Based Polyaniline Flexible Papers as Sustainable Microwave Absorbers in the X-Band, ACS Appl. Mater. Interfaces. 10 (2018) 20032–20043.
[19] A.R. Pai, T. Binumol, D.A. Gopakumar, D. Pasquini, B. Seantier, N. Kalarikkal, S. Thomas, Ultra-fast heat dissipating aerogels derived from polyaniline anchored cellulose nanofibers as sustainable microwave absorbers, Carbohydr. Polym. 246 (2020) 116663.
[20] Y. Qiao, C. Zhang, F. Kong, Q. Zhao, A. Kong, Y. Shan, Activated biochar derived from peanut shells as the electrode materials with excellent performance in Zinc-air battery and supercapacitance, Waste Manag. 125 (2021) 257–267.
[21] L. Rao, X. Lu, L. Xu, Y. Zhu, T. Xue, Y. Ge, Z. Duan, X. Duan, Y. Wen, J. Xu, Green synthesis of kudzu vine biochar decorated graphene-like MoSe2 with the oxidase-like activity as intelligent nanozyme sensing platform for hesperetin, Chemosphere. 289 (2022) 133116.
[22] S. Li, A. Huang, Y.J. Chen, D. Li, L.S. Turng, Highly filled biochar/ultra-high molecular weight polyethylene/linear low density polyethylene composites for high-performance electromagnetic interference shielding, Compos. Part B Eng. 153 (2018) 277–284.
[23] F. Natalio, T.P. Corrales, Y. Feldman, B. Lew, E.R. Graber, Sustainable Lightweight

Biochar-Based Composites with Electromagnetic Shielding Properties, ACS Omega. 5 (2020) 32490–32497.
[24] M.E. Baginski, D.L. Faircloth, M.D. Deshpande, Comparison of two optimization techniques for the estimation of complex permittivities of multilayered structures using waveguide measurements, IEEE Trans. Microw. Theory Tech. 53 (2005) 3251–3259.
[25] A.R. Pai, N.P. Azeez, B. Thankan, N. Gopakumar, M. Jaroszewski, C. Paoloni, N. Kalarikkal, S. Thomas, Recent Progress in Electromagnetic Interference Shielding Performance of Porous Polymer Nanocomposites—A Review, Energies. 15 (2022) 3901.
[26] K. Ahmed, M. Hasan, J. Haider, Electrical and mechanical properties of sugarcane bagasse pyrolyzed biochar reinforced polyvinyl alcohol biocomposite films, J. Compos. Sci. 5 (2021) 249.
[27] K.C. Choi, E.K. Lee, S.Y. Choi, S.J. Park, Electrical and physical properties of magnetite-filled NBR, Polym. 27 (2003) 40–45.
[28] X. Wu, C. Lu, H. Xu, X. Zhang, Z. Zhou, Biotemplate synthesis of polyaniline@cellulose nanowhiskers/natural rubber nanocomposites with 3D hierarchical multiscale structure and improved electrical conductivity, ACS Appl. Mater. Interfaces. 6 (2014) 21078–21085.
[29] A.C. Lua, T. Yang, Effects of vacuum pyrolysis conditions on the characteristics of activated carbons derived from pistachio-nut shells, J. Colloid Interface Sci. 276 (2004) 364–372.
[30] C.T.C. Wan, D. López Barreiro, A. Forner-Cuenca, J.W. Barotta, M.J. Hawker, G. Han, H.C. Loh, A. Masic, D.L. Kaplan, Y.M. Chiang, F.R. Brushett, F.J. Martin-Martinez, M.J. Buehler, Exploration of Biomass-Derived Activated Carbons for Use in Vanadium Redox Flow Batteries, ACS Sustain. Chem. Eng. 8 (2020) 9472–9482.
[31] H.N. Cheng, K. Kilgore, C. Ford, C. Fortier, M.K. Dowd, Z. He, Cottonseed protein-based wood adhesive reinforced with nanocellulose, J. Adhes. Sci. Technol. 33 (2019) 1357–1368.
[32] X. Xiao, B. Chen, A Direct Observation of the Fine Aromatic Clusters and Molecular Structures of Biochars, Environ. Sci. Technol. 51 (2017) 5473–5482.
[33] F. D'Apuzzo, A.R. Piacenti, F. Giorgianni, M. Autore, M.C. Guidi, A. Marcelli, U. Schade, Y. Ito, M. Chen, S. Lupi, Terahertz and mid-infrared plasmons in three-dimensional nanoporous graphene, Nat. Commun. 8 (2017) 1–7.
[34] M.J. Frisch, Gaussian 16, revision A3; Gaussian, Inc.: Wallingford,CT, (2016).

[35] T. Stein, L. Kronik, R. Baer, Reliable prediction of charge transfer excitations in molecular complexesusing time-dependent density functional theory, J. Am. Chem. Soc. 131 (2009) 2818–2820.
[36] A. Bruner, S. Hernandez, F. Mauger, P.M. Abanador, D.J. LaMaster, M.B. Gaarde, K.J. Schafer, K. Lopata, Attosecond Charge Migration with TDDFT: Accurate Dynamics from a Well-Defined Initial State, J. Phys. Chem. Lett. 8 (2017) 3991–3996.
[37] J. Chaudhary, Aarzoo, R. Roy, R.K. Roy, Screening the Band Shape of Molecules by Optimal Tuning of Range-Separated Hybrid Functional with TD-DFT: A Molecular Designing Approach, J. Phys. Chem. A. 126 (2022) 5252–5264.
[38] R.L. Martin, Natural transition orbitals, J. Chem. Phys. 118 (2003) 4775–4777.
[39] D. Tsokkou, C.Y. Cheng, N. Krainova, S. Mukhopadhyay, N.C. Giebink, N. Banerji, Ultrafast Charge Transfer Dynamics at the Origin of Photoconductivity in Doped Organic Solids, J. Phys. Chem. C. 125 (2021) 7086–7096.
[40] F.-W. Gao, H.-L. Xu, Z.-M. Su, Tuning Second-Order Nonlinear Optical Properties of Cross-Linked Carbon Nanotube via External Electric Field, J. Phys. Chem. C. 124 (2020) 3778–3783.